Nuclear Instruments and Methods in Physics Research A 1092 (2026) 171767

Contents lists available at ScienceDirect

Nuclear Inst. and Methods in Physics Research, A

journal homepage: www.elsevier.com/locate/nima

Full Length Article

A new detection array for underground charged particle spectroscopy at LUNA-400

L. Barbieri [a], J.J. Marsh [a], C.G. Bruno [a,*], M. Aliotta [a], C. Ananna [b,c], F. Barile [d,e], D. Bemmerer [f], A. Best [b,c], R. Biasissi [g,h], A. Boeltzig [f,1], R. Bonnell [a], C. Broggini [h], A. Caciolli [g,h], M. Campostrini [i], F. Casaburo [l,m], F. Cavanna [j], T. Chillery [n], G.F. Ciani [e], P. Colombetti [j], A. Compagnucci [a], P. Corvisiero [l,m], L. Csedreki [o], T. Davinson [a], R. Depalo [p,q], L. Dalla Vedova [a], A. Di Leva [b,c], Z. Elekes [o,r], F. Ferraro [n], A. Formicola [s], Zs. Fülöp [o], G. Gervino [j,k], R.M. Gesuè [n], G. Gosta [p,q], A. Guglielmetti [p,q], C. Gustavino [s], Gy. Gyürky [o], G. Imbriani [b,c], J. Jones [a], M. Junker [n], M. Lugaro [t], E. Masha [f], R. Menegazzo [h], D. Mercogliano [b,c], D. Piatti [h,g], P. Prati [l,m], D. Rapagnani [b,c], V. Rigato [i], D. Robb [a], M. Rossi [l,m], R. Sariyal [j], R.S. Sidhu [a,2], J. Skowronski [g,h], O. Straniero [u], T. Szücs [o], S. Turkat [f], M. Vagnoni [s,v], S. Zavatarelli [m]

[a] *School of Physics and Astronomy, The University of Edinburgh, JCMB, Peter Gurthrie Tait Road, Edinburgh, EH9 3FD, United Kingdom*
[b] *Università degli Studi di Napoli "Federico II", Dipartimento di Fisica"E. Pancini", Via Cintia, Napoli, 80126, Italy*
[c] *INFN, Sezione di Napoli, Via Cintia, Napoli, 80126, Italy*
[d] *Università degli Studi di Bari, Bari, 70125, Italy*
[e] *INFN, Sezione di Bari, Bari, 70125, Italy*
[f] *Helmholtz-Zentrum Dresden-Rossendorf, Dresden, Germany*
[g] *Dipartimento di Fisica e Astronomia, Università degli Studi di Padova, Via F. Marzolo 8, Padova, 35131, Italy*
[h] *INFN, Sezione di Padova, Via F. Marzolo 8, Padova, 35131, Italy*
[i] *INFN Laboratori Nazionali di Legnaro, Via dell'Università 2, Legnaro (PD), 35020, Italy*
[j] *INFN, Sezione di Torino, Via P. Giuria 1, Torino, 10125, Italy*
[k] *Università degli Studi di Torino, Torino, Italy*
[l] *Università degli Studi di Genova, Via Dodecaneso 33, Genova, 16146, Italy*
[m] *INFN, Sezione di Genova, Via Dodecaneso 33, Genova, 16146, Italy*
[n] *INFN Laboratori Nazionali del Gran Sasso, Assergi (AQ), Italy*
[o] *HUN-REN ATOMKI Institute for Nuclear Research, Debrecen, Hungary*
[p] *Università degli Studi di Milano, Via Celoria 16, Milano, 20133, Italy*
[q] *INFN, Sezione di Milano, Via Celoria 16, Milano, 20133, Italy*
[r] *Institute of Physics, Faculty of Science and Technology, University of Debrecen, Debrecen, Hungary*
[s] *INFN, Sezione di Roma, Piazzale A. Moro 2, Roma, 00185, Italy*
[t] *Konkoly Observatory, Research Centre for Astronomy and Earth Sciences, HUN-REN CSFK, Budapest, 1121, Hungary*
[u] *Osservatorio Astronomico di Collurania, Teramo, Italy*
[v] *Dipartimento di Matematica e Fisica, Università della Campania "L. Vanvitelli", Viale Lincoln, 5, Caserta, Italy*

ARTICLE INFO

Keywords:
Nuclear astrophysics
Underground physics
Silicon detectors

ABSTRACT

Nuclear astrophysics experiments at low energies greatly benefit from the background reduction afforded by deep underground laboratories, allowing the detection of rare events from low-probability nuclear reactions. While the advantages of this approach are well-known for reactions emitting photons, this strategy has been exploited less for reactions emitting exclusively charged-particles. Here, we report on the construction and commissioning of a new charged-particle detection array designed for measurements of nuclear reactions at

---

* Corresponding author.
E-mail address: carlo.bruno@ed.ac.uk (C.G. Bruno).

[1] Current address: Physikalisch-Technische Bundesanstalt (PTB), Braunschweig, Germany.

[2] Current address: University of Surrey, Guildford, UK.

https://doi.org/10.1016/j.nima.2026.171767
Received 25 March 2026; Received in revised form 23 May 2026; Accepted 11 June 2026

the LUNA-400 accelerator, located deep underground in INFN Laboratori Nazionali del Gran Sasso (Italy). We describe the challenges and requirements for this array, and report on its performance for future physics studies.

1. Introduction

Direct investigations of nuclear reactions relevant for astrophysics are often hampered by the effect of the Coulomb barrier, which greatly reduces the cross-section at energies of stellar interest. On the Earth's surface, rare events produced by these nuclear reactions are extremely challenging or even impossible to distinguish from the natural and cosmic radiation background. Performing experiments underground, to suppress these background contributions for nuclear reaction measurements, was pioneered by the Laboratory for Underground Nuclear Astrophysics (LUNA) experiment, located in INFN Laboratori Nazionali del Gran Sasso (Italy). The underground LUNA 400 kV accelerator is capable of delivering high-intensity (> 100 μA) beams of protons or α-particles at proton energies E_{beam} = 40–400 keV, ideally suited for nuclear astrophysics, onto solid or gaseous targets. Historically, LUNA focused on nuclear reactions producing γ-rays, detected using large-volume High Purity Germanium detectors [1], or a BGO scintillator array [2]. Both detector types can be shielded with low-activity lead to further reduce the natural background. LUNA has been employing this approach to carry out a wide range of successful experimental campaigns investigating scenarios from the Big Bang [3], to AGB Stars [4,5], and Globular Clusters [6,7]. More recently, LUNA carried out the first-ever study of underground in-beam neutron spectroscopy using a purpose-built neutron detection array [8], probing the ^{13}C(α,n) reaction, a key neutron source in the slow-capture neutron process [9]. Following from the success of LUNA, other underground accelerators have been built around the world: the Felsenkeller accelerator in Germany [10], the Jinping Underground Nuclear Astrophysics (JUNA) in China [11,12] and the Compact Accelerator System for Performing Astrophysical Research (CASPAR) in the USA [13].

Underground measurement of reactions producing γ-rays and neutrons is a well-established and successful technique. However, several nuclear reactions of key importance for nuclear astrophysics produce exclusively charged-particles, such as *e.g.* the ^{23}Na(p, α)^{20}Ne nuclear reaction of key importance in Globular Clusters [14]. These reactions cannot be investigated with extant setups at LUNA, and a different approach is required: underground in-beam charged-particle spectroscopy. This is a relatively new and unexplored technique, with a pioneering first measurement performed at LUNA-50 [15] and a more comprehensive study using silicon detectors carried out later at LUNA-400, which reported up to an order of magnitude background reduction [16]. This advantage was exploited for the subsequent measurements of the astrophysically crucial ^{17}O(p, α)^{14}N [17] and ^{18}O(p, α)^{15}N [18] reactions, which had major implications in our understanding of AGB stars [19–21]. In this work, we report on the construction and commissioning of a new beamline and particle detection setup designed for studies of nuclear reactions emitting charged-particles at LUNA. The array was designed to have the highest possible geometric efficiency, so as to maximise the counting rate from the rare events to be investigated, while still retaining some angular resolution, and being compatible with the measurement conditions at LUNA. For example, the typical beam intensity at LUNA-400 (100–300 μA) paired with long measurement times (weeks to months), require thick, rugged, water-cooled targets that can be smoothly replaced at frequent intervals (typically a few times per week). Such high beam intensities, necessary to increase the rare event rate, produce a high flux of elastically backscattered ions, from which the particle detectors need to be protected. Additionally, whenever changing the target, the reaction chamber is exposed to the humid and dusty underground environment. In this paper, we present how these and other issues were tackled.

2. The new beamline

2.1. Overview

Fig. 1 shows the new experimental setup constructed and commissioned at LUNA-400. The ion beam from the LUNA-400 accelerator is directed in a straight beamline via a dipole magnet. Ions pass through a set of rastering magnets (Section 2.3) that increase the size of the beam to spread its power over a larger area, reducing damage to the target. The beam then passes through a long copper cold finger (Section 2.4) that also acts as a collimator and enters the reaction chamber (Section 3). Here, ions impinge on a solid target that also acts as the beam stop.

2.2. Pumping system

A new beamline (Fig. 1) was constructed and installed at LUNA-400. The beamline was built from 304 stainless steel and installed in place using surgical gloves to avoid contamination by the oils in human skin. Exposed surfaces were cleaned with acetone to further reduce any potential contamination. A vacuum level of $7-9\times10^{-7}$ mbar, sufficient to minimise the chances of in-vacuum contamination and carry out our measurement, is achieved in a few hours via a single multi-stage roots pump (Pfeiffer Vacuum ACP40) connected to two Agilent turbo-molecular pumps (TwisTorr 305 FS and TwisTorr 74 FS). The vacuum levels are monitored via a Bourdon gauge and an Edwards wide range vacuum head. When the cold trap (Section 2.4) is filled, it acts as a cryogenic pump, and the pressure in the beamline can further decrease to 4×10^{-7} mbar. To prevent condensation and humidity from entering the chamber when changing the target, dry nitrogen is kept flowing for the duration of the procedure, maintaining the beamline in overpressure until the chamber is closed again. Using this approach, with a filled cold trap, a vacuum level of 10^{-7} mbar is recovered after ~30 min after changing the target.

2.3. Rastering magnets

A large amount of power is deposited by the ion beam onto the target. If the illuminated target area is very narrow, this concentrated power can quickly degrade the target and cause severe damage. It is therefore crucial to spread the beam power over the largest possible area. In our setup, the expected beam diameter at the exit of the accelerator tank is of the order of $d\sim5$ mm. To mitigate target damage from the resulting exceedingly small beam spot, two sets of custom-built electromagnets were installed downstream of the dipole magnet. These are used to raster the beam in the two directions perpendicular to its axis. Rastering is done by driving the current flowing in the two sets of magnets using two independent sinusoidal signals having frequencies 7.3 Hz (vertical), and 3.6 Hz (horizontal). This technique allows to raster the $d\sim5$ mm beam spot resulting in a uniformly illuminated $d\sim17$ mm area at the target position. As shown in Fig. 2, under these conditions the beam spot effectively covers almost the entire target area, allowing sufficient power dissipation to prevent target damage. In addition to rastering, these magnets can also be used to bend the beam via an offset to the driving signal, which provides an additional way to place the beam on target.

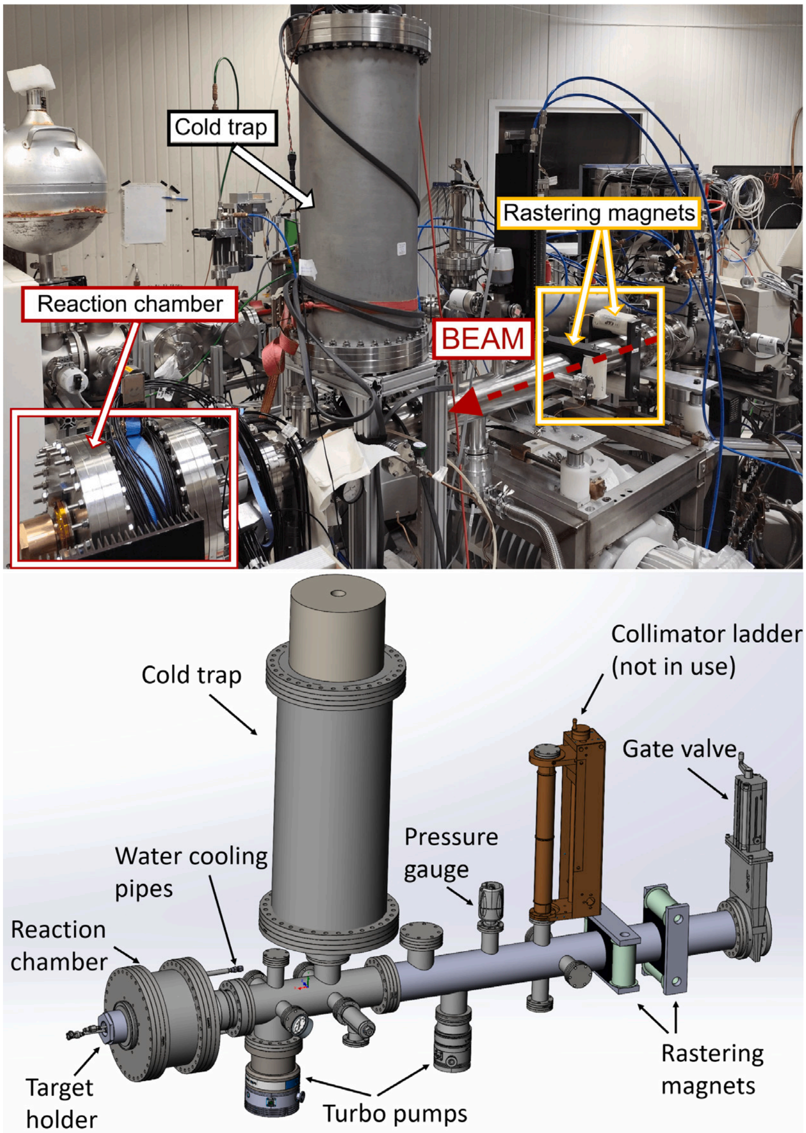

Fig. 1. (Top) A picture of the new beamline and reaction chamber. (Bottom) A 3D render of the setup. The beam from the LUNA-400 accelerator is focused via a dipole, rastered via two sets of magnets, and reaches the solid target passing through a copper cold finger connected to a cold trap. See text for more details.

2.4. Cold trap and cold finger

Carbon deposition by the ion beam on the surface of the target is a well-known issue affecting the accuracy of nuclear reaction measurements. A cold trap is an extremely effective way to reduce this deposition to a negligible level by providing a colder surface where residual gas contaminants, as well as any potential contaminants released by the target when heated by the beam, can condense. Among these contaminants, carbon is a ubiquitous element. Minimising the build-up of a carbon layer on the target is crucial to avoid the consequent decrease of the effective energy at which the ions interact with the target nuclei, and progressive loss of beam energy accuracy. The cold trap employed in our setup was designed and produced in the workshop of the Helmholtz-Zentrum Dresden-Rossendorf using a similar approach to that used for the cold trap at the Felsenkeller facility [10]. It consists of a 15 litre cryostat filled with liquid nitrogen (LN_2) mounted on top of the beamline. In an effort to minimise the loss of LN_2 over time, the vacuum insulation for the cryostat was designed to be part of the same vacuum volume as the beamline. This results in the mechanical connection between the cryostat and the cold finger occurring entirely under vacuum, as shown in Fig. 3. This is unlike other cold traps employed at LUNA-400 [16], where the cryostat-cold finger connection penetrates through the vacuum envelope around the cryostat, reducing thermal insulation. Experimentally, we did not observe significant differences in LN_2 evaporation rate between the two approaches. Both designs, which have comparable volumes, have a 24 h refill cycle, with or without beam on target.

The cold trap is mechanically connected to a cold finger via a thick copper block lined with an indium foil for effective thermal contact. The cold finger is an Oxygen-Free High-thermal Conductivity (OFHC) copper tube placed coaxially in the centre of the beamline. It is 500 mm long and has a 24 mm inner diameter, tapering down to a 22 mm diameter tube in the last 100 mm. The cold finger slots mechanically into the silver dome (Section 3.3). Because of its length and position, the cold finger, together with the copper block that holds it in place, also acts as a collimator for the ion beam.

3. Reaction chamber and detection array

3.1. Overview

A sketch of the reaction chamber is shown in Fig. 4. The beam travels inside the cold finger (Section 2.4), through a ceramic vacuum

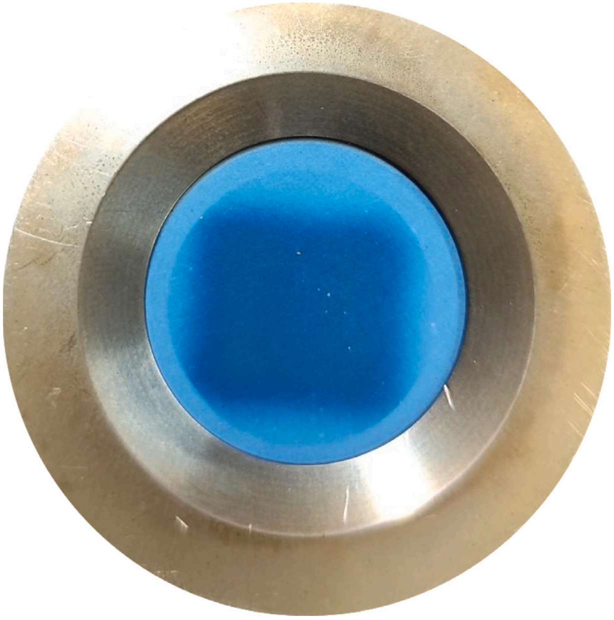

Fig. 2. A picture of a typical beamspot (darker blue shade) after rastering perpendicular to the beam axis. The size of the beamspot is approximately 17×17 mm^2. The target holder is described in Section 3.2.

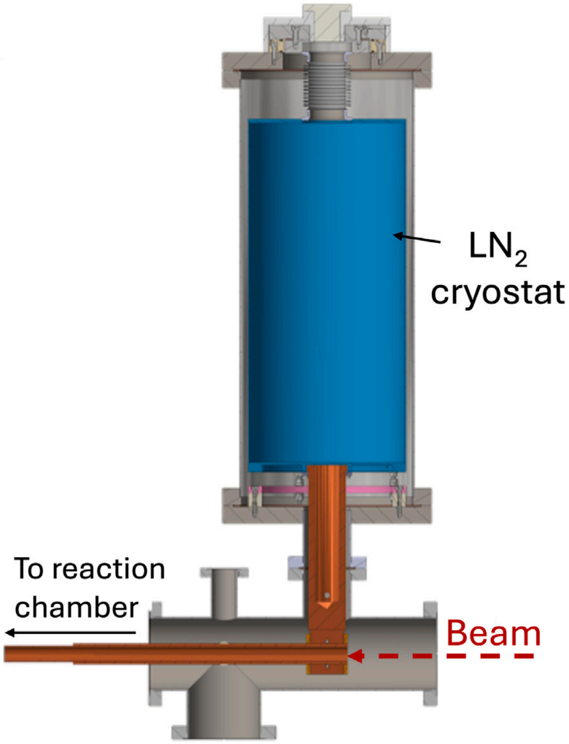

Fig. 3. A sketch of the custom-made cold trap. A liquid nitrogen reservoir is placed in a cryostat on top of the beamline, connected to an OFHC copper finger placed coaxially inside. The beam passes through the cold finger, which acts as a collimator. See text for details.

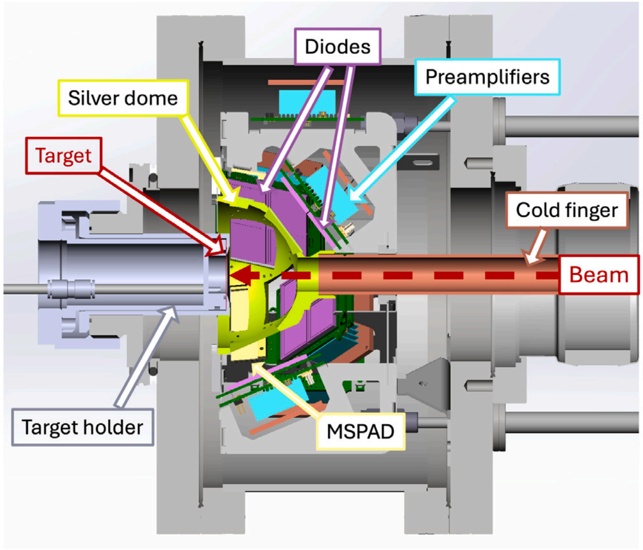

Fig. 4. A sketch of the reaction chamber showing the cold finger, silver dome, detectors, preamplifiers, and target holder with target. See text for details.

break, and into the reaction chamber. The ceramic break separates the electrical ground of the reaction chamber from that of the beamline. Once in the chamber, the ions travel through a silver dome (Section 3.3), and hit the solid target held in place by the target holder (Section 3.2). Charged particles emitted at backwards angles in the laboratory frame travel through thin foils (Section 3.4) held onto the silver dome, past a grounding mesh-grid dome (Section 3.5) and are finally detected by an array of silicon detectors. This array comprised of 24 Hamamatsu Photodiodes (Section 3.6) and 3 Micron Semiconductor Ltd 1×5 pad detectors (MSPAD) (Section 3.7). The detector signals are processed by RAL108 preamplifiers (Section 3.8) and sent to a set of CAEN VME digitisers (Section 3.9) that comprise the Data Acquisition System.

3.2. Target holder

The very high ion beam intensities (100–300 μA) at LUNA-400 can cause significant damage to solid targets, especially when irradiating them for up to several days without interruption. In addition to the rastering of the beam, which spreads the power over a larger surface area and reduces target damage (see Section 2.3), target cooling is also required to significantly reduce their degradation and avoid mechanical damage to the backings due to overheating. Even with these precautions, targets typically have to be replaced every few days to few weeks, depending on the type. A full discussion of the durability under beam of targets mounted on this beamline will be reported in a future article. Target degradation mandates the use of relatively large-area targets placed in water-cooled target holders that can be quickly replaced to reduce the time during which the vacuum chamber and the LN$_2$ cooled copper finger remain exposed to the outside environment. The solution we employed is shown in Fig. 5. The target holder is comprised of two stainless steel cylinders, an inner and an outer one. The inner is connected to a Julabo FP50 recirculating chiller that continuously provides water cooled to 8 °C through detachable water hoses. The target is placed on top of this cylinder with a Viton O-ring forming a seal between the circulating water and the target itself. The water-cooled inner cylinder is slid into the outer one and the two are fastened together. A Viton O-ring between the cylinders provides vacuum sealing of the whole assembly. The target holder is held in place by a threaded flange, screwed on the downstream flange on the air side. When changing target, the threaded flange is unscrewed, the target holder is extracted, a second target holder with a fresh target is inserted, and the flange is screwed on again before restarting the pumps. This entire procedure can be completed in seconds. The flange on which the target holder is mounted is electrically insulated from the

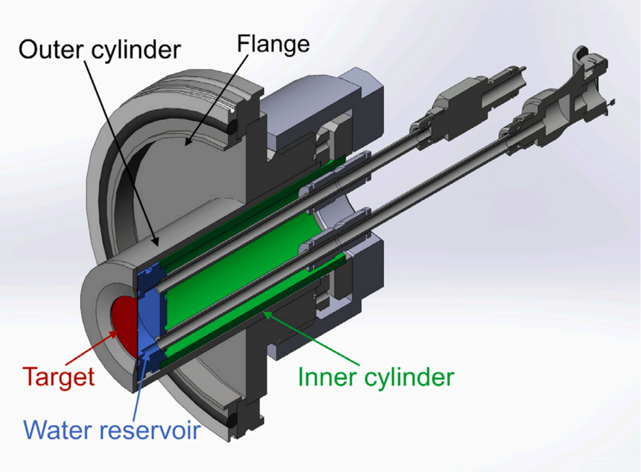

Fig. 5. A cut-away 3D render showing the target holder designed for this experiment. To change the target, the inner and outer cylinder assembly is detached from the flange. The inner cylinder is removed from the outer cylinder, allowing the irradiated target to be replaced with a fresh one. The cylinders are then reassembled and remounted onto the flange. See text for more details.

rest of the reaction chamber via a plastic centring ring and insulating Kapton tape. This turns the target into a Faraday cup, allowing a precise measurement of the ion beam current. The integrated current value is recorded via a CAEN N1145 scaler. Prior tests of the amperometer observed a 3% systematic uncertainty on the current reading [22].

3.3. Silver dome

The interaction of the intense ion beam with the target produces a very significant flux of back-scattered ions, along with a large number of secondary electrons. This effect is further enhanced for targets and backings with high-Z isotopes, for example the tantalum backing typically used at LUNA. This back-scatter radiation would be sufficient to destroy the detectors in the span of minutes to seconds, while secondary electron emission would affect the accuracy of the current measurement and increase detector noise. To solve both of these issues, we designed a dome, made of a thermally and electrically conductive material, to be installed upstream of the target. The dome can be biased to -200V to provide a uniform electrostatic field repelling the secondary electrons back into the target. Moreover, the dome has holes corresponding to the position of the detectors on which thin foils can be mounted. The thickness of these foils can be chosen to stop the recoiling beam ions, while letting through the particles produced by the reaction of interest. Finally, the dome can be connected to the cold finger, allowing the foils to constantly dissipate some of the heat deposited by back-scattered particles.

Designing the dome posed several challenges since it requires a balance between geometric efficiency, lifetime of the protective foils under beam, and angular resolution of the setup. To maximise the efficiency, a large number of detectors in close proximity to the target is needed. This requires large holes in the dome, covered by thin foils to protect the detectors. Foils have poor thermal conductivity and can suffer heat damage and break during irradiation. Smaller area foils more easily dissipate heat, but result in lower geometric efficiency. A compromise between these considerations resulted in the dome shown in Fig. 6. The dome features six square holes of $30\ x\ 30\ \text{mm}^2$ each and three rectangular holes of $12 \times 35\ \text{mm}^2$ each. The expected geometrical efficiency of this compact setup was determined following the approach described in Section 4.3.

We decided to fabricate the dome via investment casting. The shape of the dome was 3D printed using a Anycubic Photo Mono X 6K printer in Siraya Tech Cast castable resin. The resin was brought to the School of Sculpture in the Edinburgh College of Art, where it was coated in a thick layer of SRS-brand classic investment. Before application, the liquid investment was placed under mechanical vacuum to remove air bubbles and increase the quality of the cast. Holes and channels were left in the cast, through which the molten metal could later be poured in. After the investment dried, the cast was heated to roughly 600° Celsius for ~2 days in an oven in order to burn away the resin, leaving a dome-shaped cavity in the cast. The cast was then taken out of the oven, and molten silver was poured in. Silver was chosen instead of OFHC copper as the latter would not remain oxygen-free if molten and solidified in air. After cooling down, the investment material was removed, and the dome was cleaned, polished, and threaded holes to mount foils were added. Fig. 6 shows the finished solid silver dome.

3.4. Protective foils

Beam ions elastically back-scattered from the target would quickly destroy silicon detectors upon hitting them; hence, protective foils are mounted on the silver dome. Their thickness is carefully chosen to stop the back-scattered ions while still letting the reaction products through with detectable energy. The optimal material and thickness vary depending on the nuclear reaction of interest. To ensure a complete suppression of the secondary electrons and to improve heat dissipation, foils should be made of conductive material or at least have a layer of conductive material deposited on them, facing the target. For example, for the first reaction studied with this setup, ^{23}Na(p, α)^{20}Ne, aluminised Mylar foils approximately $3.5\ \mu\text{m}$ thick were chosen. We observed experimentally the Mylar in the foils degrading with time when beam was on, turning into a dark shade of yellow. No failures occurred during beam time. Still, based on prior experience [16] we routinely replaced all foils every ≈8 weeks of beam on target to prevent any sudden foil failure from damaging the detectors.

3.5. Mesh grid dome

We observed a substantial increase in electronic noise, and a decrease in resolution, when the silver dome was mounted in front of the detectors (Section 4.2). Note that this was observed without beam, and without any other changes to the setup. To reduce this effect, we mounted fine mesh grids (50-Mesh T316, Stainless Steel, High-Transparency, 0.0012" wire diameter) on a stainless steel dome (Fig. 6, bottom left) placed between the silver dome and the silicon detectors. This dome is firmly grounded via a copper wire and breaks the lines of the electromagnetic field, shielding the detectors, reducing the electronic noise and enhancing the resolution, as also discussed in Section 4.2. The fine mesh grids decrease the geometric efficiency to around 89% of the nominal total, purely due to shadow effects. This reduction was determined experimentally by measuring the decrease in the measured counts from a ^{241}Am/^{244}Cm/^{239}Pu triple-α source placed in front of a Hamamatsu Si PIN diode, with and without the mesh.

3.6. Diodes

Six assemblies consisting of four Hamamatsu S3204-09 Si PIN diodes each, were installed at backwards angles around the target, as shown in Fig. 7. These detectors were chosen for their ruggedness and low-cost and the possibility of fitting them in a compact setup, maximising detection efficiency while retaining some angular resolution. Diodes operate in reverse-bias mode, with a voltage of −60 V applied to the p+n junction side with respect to the n+n side which was kept to ground (0 V). Each diode features an active area of 324 mm^2 and an active thickness of 0.3 mm. Signals can be read from both the p+n junction side facing the target, and the n+n ohmic side facing away from the target. Each set of four diodes is soldered onto a Printed Circuit Board (PCB), described in Section 3.8. The detectors are

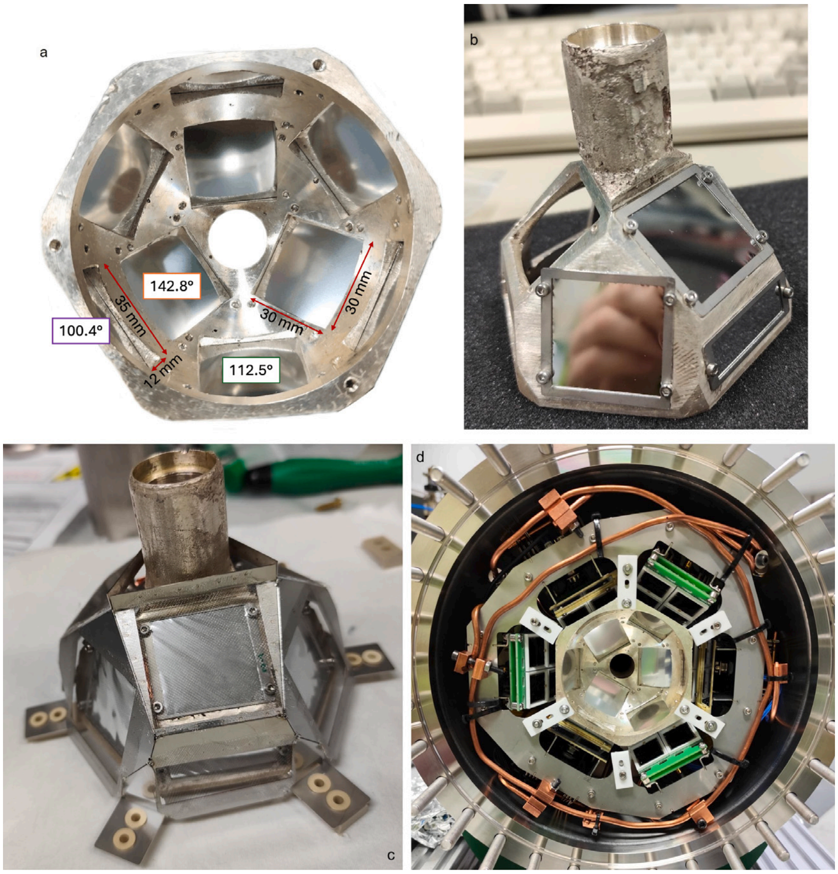

Fig. 6. (a–b) Two views of the silver dome with the protective foils mounted. The holes sizes and angles with respect to a plane located 5 mm above the dome basis are reported. (c) View of the outer dome supporting the fine mesh grids used to break the electromagnetic field lines between the silver dome and the detectors. The silver dome is visible beneath. (d) View of the dome mounted in the reaction chamber and held in place by a set of MACOR spacers.

mounted at a nominal fixed distance of 60 mm from the centre of the target by fastening their PCBs on the stainless-steel support structure visible in Fig. 7. This arrangement places them at a distance of about 17 mm from the six square holes in the dome, and allows the detection of particles at four angles with respect to the beam axis (102.1°, 125.7°, 130.1°, and 154.5°). Each diode covers approximately 17° × 17°.

3.7. MSPADs

To further increase the detection efficiency, three Micron Semiconductor Ltd. MSPADs 1 × 5 were also installed in the array. These have been chosen as their smaller size and rectangular shape allowed them to fit into otherwise unused spaces within the setup. MSPADs are neutron Transmutation Doped (nTD) [23] double-sided silicon detectors with four 100 mm^2 independent pads, and a narrower 8 mm^2 central pad, for a total active area of 408 mm^2 with 0.5 mm thickness. The MSPADs are biased at −90 V, and signals are read from both sides of the four larger pads. The central pad was not useful for this application, and left disconnected. A PT100 sensor is located on one side of the detector carrier, as shown in Fig. 8. The MSPADs are mounted on the same stainless steel support structure as the diodes, aligned with the rectangular openings of the dome and positioned at the same distance of about 60 mm from the target (see Fig. 7). The associated detection angle is centred at 102.5° with respect to the beam axis, covering approximately 10° × 40°. A Kapton ribbon cable connects each MSPAD to a PCB (see Figs. 8 and 9).

3.8. Preamplifiers

Signals from all detectors are processed via a system of custom-made PCB pairs. The PCBs in the pair (see Fig. 9) are connected to

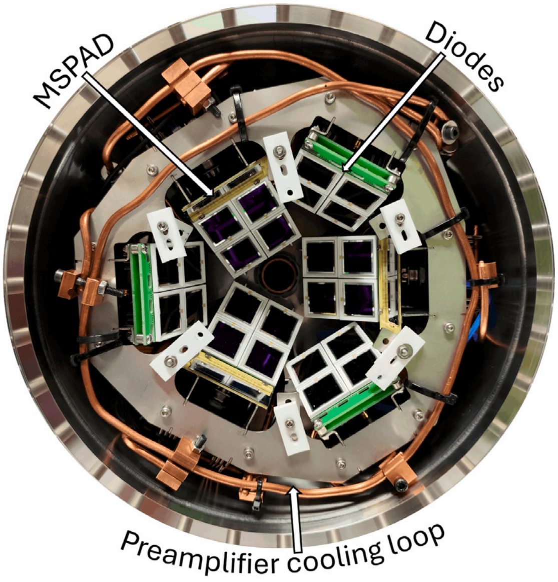

Fig. 7. A photograph showing the inside of the reaction chamber with the full detection array mounted. The Hamamatsu diode assemblies are visible (black squares), as well as the three MSPADs (rectangular reflecting pads with pale yellow carriers). The cooling pipe for the preamplifiers (Section 3.8) can also be seen looping around the detectors support structure. See text for details.

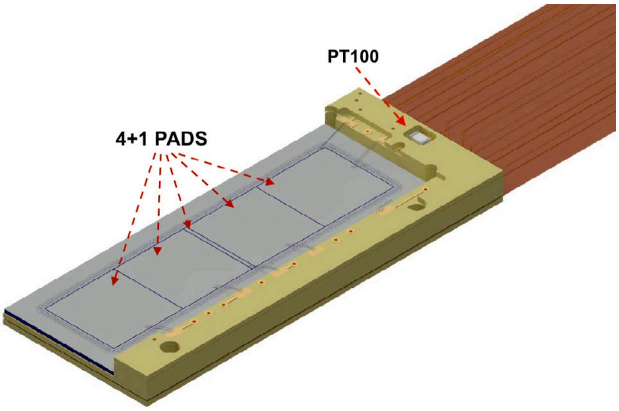

Fig. 8. Technical drawing of an MSPAD with its 4 square PADs, central narrow PAD and the yellow carrier where a PT100 sensor is located. The orange Kapton ribbon cable for the PCB connection is also partially visible.

each other via a sub-D connector. There are six PCB pairs for the diode assemblies, and three PCB pairs for the MSPADs. Detectors are connected to the front PCB of the pair, which has different designs for the diodes and the MSPADs. In particular, the front PCB for the diodes hosts four PT100 temperature sensors behind each diode. The rear PCB has the same design for both detector types, and houses eight RAL108 preamplifiers (10 mV/MeV sensitivity into 100 Ω [24]). Four preamplifiers process the negative signals from the n+n detectors sides, and another four process the positive signals from the p+n sides. The nine board pairs are ultimately connected to three internal breakout PCBs, each providing routing for two diode assemblies and one MSPAD. Signals from these three internal breakout PCBs are further routed to three external breakout PCBs via vacuum feed-throughs. The internal and external breakout PCBs are used to extract the signals from the reaction chamber. There are $2 \times 6 \times 4$ channels for the diodes, and $2 \times 3 \times 4$ channels for the MSPADs, for a total of 72 channels. Additionally, the breakout boards distribute the bias to the detectors, power the preamplifiers, and feed a test input to all channels. They also route the signals from the PT100 sensors located on the diodes front boards, and the PT100 sensor on the MSPAD. The PT100 resistance readings can be converted into temperature values with a PT100 reader, allowing us to monitor temperature changes.

The advantage of having the preamplifiers under vacuum is that the path connecting detectors and preamplifier is minimised. This is the part of the electronic chain most sensitive to noise. Minimising its length should improve the detection resolution, and reduce the sensitivity to extrinsic noise sources. However, each of the 72 preamplifiers dissipates approximately 230 mW during operation. Under vacuum, this heat load rapidly leads to a significant temperature increase of the surrounding components, reaching an equilibrium around 80 °C. This not only enhances outgassing from the PCB materials, but also creates a local heat source in close proximity to the silicon detectors, which are highly sensitive to temperature. Ultimately, high temperature leads to high leakage currents, and a degradation in energy resolution. An in-vacuum cooling system was therefore designed.

A laser-cut copper plate is attached to the back of each preamplifier using epoxy resin, creating a thermal exchange interface. Each plate has a slot where a cooling pipe can be inserted. Sealed copper heat pipes, each independently filled with low pressure water, are inserted in each slot and secured with a copper clip to a longer cooling water copper tube, which loops around the detector support structure. The cooling loop is visible in Fig. 7. Water at 8 °C is continuously pumped in the cooling loop by the same chiller used for cooling the target, removing the heat produced by the preamplifiers. The combined action of the cooling system and the LN_2-cooled silver dome results in an equilibrium temperature for the detectors of around 42 °C while kept under vacuum. After a target-swap, the temperature is recovered in around 20 min. We observed that cooling the array at temperatures below ∼ 45 °C was sufficient to lower the thermal noise to a level suited for our measurements, improving the system resolution by about 30% (Section 4.2) and ensuring its long-term stability.

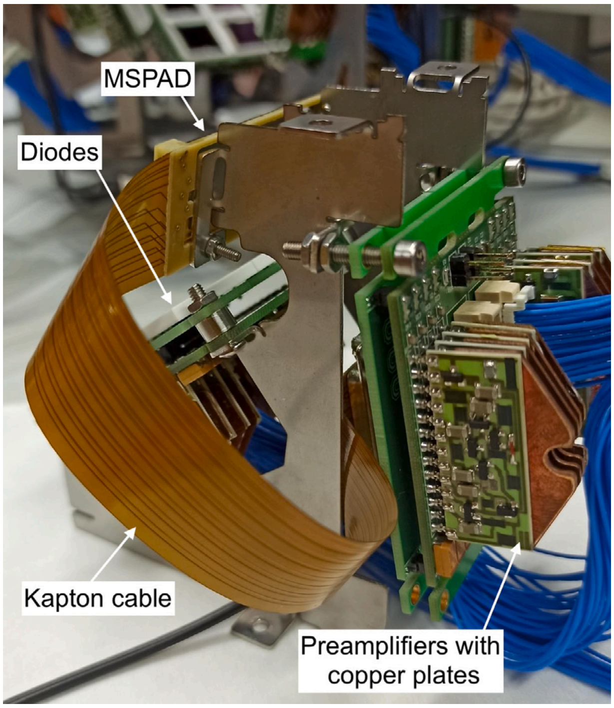

Fig. 9. A photograph of a detector support structure housing four diodes and one MSPAD, and their PCBs. The back of the MSPAD carrier is visible in pale yellow at the top. The Kapton ribbon cable connects the MSPAD to its front PCB, which is connected to the rear PCB where eight RAL108 preamplifiers are inserted. Copper plates are glued to the back of the preamplifiers, with a slot for the cooling pipes. Below the MSPAD, some of the diodes' white carriers can be seen, as well as their PCB pair. The blue ribbon cables are used to route the signals to the breakout PCB.

3.9. *Data acquisition system*

Pre-amplified signals are digitised by five 14 bit CAEN VME digitisers (four 16-channel V1730SB and one 8-channel V1730SD) running PHA firmware with 500 MS/s sampling rate. Data from each channel are sent via optic fibre link to an acquisition PC through a CAEN V1718 USB-CONET bridge. The CAEN CoMPASS software is used to save acquired events in list mode for further processing. The software utilises a Trapezoidal Filter for signal energy determination and a Trigger and Timing Filter to perform a digital RC-CR2 filter, identify input signals, and evaluate their timestamps. Trapezoid parameters were set to a rise time of 1.6 μs and a flat top of 0.8 μs, while the RC-CR2 signal rise time was 80 ns with a smoothing of 128 samples. These parameters were optimised to minimise the noise. A Trapezoid Decay Time (pole zero) of 26 μs was used to minimise under/over shooting of the signal when returning to its baseline.

To monitor electronic resolution and dead time, a test input signal produced by a BNC Model 9010 Programmable Pulse Generator can be fed into the electronic chain. The test signal can be configured with either polarity and the amplitude is chosen to prevent any overlap between the resulting pulser peak and the particle spectra. During the commissioning of the setup, a pulse frequency of 9 Hz was used to estimate the expected number of pulses in a given run and to derive

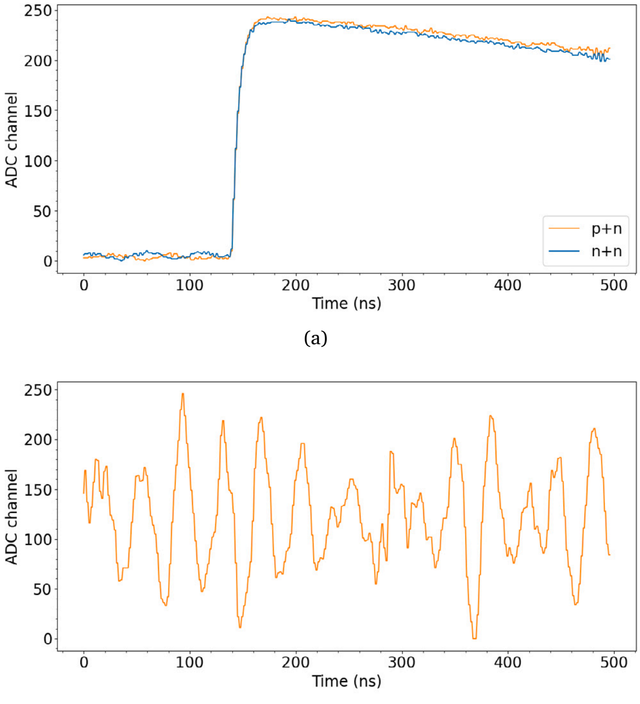

(a)

(b)

Fig. 10. Examples of recorded waveforms. A charged-particle signal seen in coincidence on the two sides (p+n and n+n) of an Hamamatsu PIN diode is shown in the top panel (a), while a noise event is visible in the bottom panel (b).

the acquisition dead time as the percentage of pulses lost in the final spectrum. Dead time was found to be less than 2%, which is sufficiently low to ensure reliable data acquisition. Overall, typical data rates are of 5–25 kB/s. Event waveforms can also be saved to disk, however, this would increase the data rate to few MB/s, which was observed to result in a significant increase of dead time. Therefore waveforms were not saved to disk except for specific test cases.

4. Commissioning results

4.1. Noise reduction algorithm

We observed an increase in event rates across all detectors when the motor generator of the LUNA-400 accelerator was turned on, and another increase when the RF frequency of the ion source was turned on. Extrinsic noise generated by these two components was the source of noise events, which is not unexpected, and was observed to be reduced by the presence of the mesh grid dome. In addition to these two noise sources, we observed a very substantial increase in event rates when the beam interacted with the solid target. While the source of this additional noise is linked to beam–target interaction, we were unable to pin down its physical origin. Using a light sensor mounted on an optical port, we excluded light produced by beam–target interaction. Given the presence of the mesh grid, the silver dome, and the foils, we expect that δ electrons should not be able to reach the detectors. Inspecting the waveforms recorded during commissioning with beam, two distinct types of signal were identified, as shown in Fig. 10. The first arises from physical events, and has a clear leading edge and defined pulse height. The second is associated with noise, and is characterised by the absence of a coherent pulse shape.

Comparing the timestamps of events recorded from the two sides of each detector, we found that signals produced by charged particles are nearly always registered in coincidence, while noise occurs randomly and shows no timing correlation between the two sides. For each acquired run, the list mode events were filtered using an algorithm that identified and kept only events recorded on both sides of a detector within a time window of 20 ns. This time corresponds approximately to the rise time of the signal of physical events. Spectra were then reconstructed using time-matched events, and p+n events were used for subsequent analysis. No appreciable differences were observed between the spectra from the two sides; however, the p+n side was chosen because the test signal used to monitor the array resolution was positive. To check the performance of the filtering algorithm and ensure real signals were not being discarded, some shorter runs with waveforms were acquired, both with an ^{241}Am α-source at approximately the target position, and with beam on target. The filtering algorithm was applied and the waveforms corresponding to the rejected events in a broad energy region of interest corresponding to the expected signal energy were separately saved. These rejected waveforms were visually inspected individually to identify any physical signal incorrectly discarded. The number of such events was found to be $\ll 1\%$. Results of this procedure are illustrated in Fig. 11, where the raw and processed spectra of a long run with proton beam at $E_p = 144$ keV on an ^{18}O target are shown (see later for more details).

4.2. Calibration and resolution

The energy calibration of the detection array was carried out using a procedure similar that described in [16]. The presence of the protective foils causes the particles emitted by any reaction from the target to undergo energy losses and straggling prior to their detection. Therefore, the pulse height of a signal does not correspond directly to the particle energy as derived from kinematics calculations. Moreover, manufacturers often quote foil thicknesses with uncertainties larger than the accuracy to which the value has to be known for our analysis. It is however possible to calibrate the detectors and derive the foil thicknesses at the same time by adopting an iterative procedure. First, the energy of the α-particles from the ^{18}O(p, α)^{15}N and ^{7}Li(p, α)^{4}He reactions and of the ^{3}He from the ^{6}Li(p, α)^{3}He reaction after passing through a foil of given thickness are calculated using SRIM [25]. Subsequently,

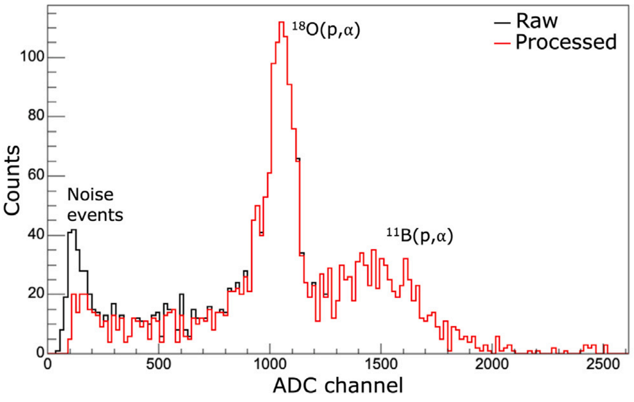

Fig. 11. Raw spectrum (black) and the corresponding processed spectrum (red) for a long run with proton beam at E_p = 144 keV on an ^{18}O target, taken by an MSPAD. The processing algorithm is described in the text.

a preliminary calibration gain is obtained using the energies of the particles emitted by the ^{6,7}Li + p reactions, and used to infer the energy of the α-particles from the ^{18}O(p, α)^{15}N reaction. This inferred energy is then compared to that predicted by SRIM, obtaining a calibration residual. This procedure is iterated for a set of thicknesses around the nominal value until a minimum in the residual is found. The calibration gain corresponding to this value of foil thickness is the final adopted one. A derived gain between 1.9 and 2.2 was determined for all the detectors, which is similar to the expected RAL108 gain of ∼2 keV/ADC channel.

To assess the energy resolution of the electronic chain, a positive test signal from a pulser was fed into the system, producing a pulser peak in the p+n sides spectra. The calibration offset was derived by varying the amplitude of the test signal, recording the ADC channel of the corresponding pulser peak, and finally extrapolating to zero a linear fit of the ADC channels to the amplitudes. Moreover, the FWHM of the pulser peak can be used to estimate the minimum electronic resolution of the electronic chain before any detector effects. With the full setup mounted, including circulating water and accelerator source on, but without beam on target, we observe a pulser FWHM of ∼20 keV on the MSPADs spectra and of ∼30 keV on the diodes. The installation of the mesh grid improves the resolution, leading to a pulser FWHM of ∼14 keV for the MSPADs and of ∼24 keV for the diodes. When beam is switched on, we observe a deterioration of the energy resolution. This effect becomes more pronounced at higher beam energies and beam currents, which we attribute to the beam interacting with the cold finger giving rise to an antenna-like emission picked up by the detectors. As a result, for E_{beam} = 150 keV, the resulting pulser FWHM is ∼40 keV for the MSPADs and ∼70 keV in the diodes. At E_{beam} = 290 keV, the value increases to ∼64 keV for the MSPADs and ∼120 keV for the diodes. A similar increase in pulser FWHM is observed when increasing the beam currents from 80 to 160 μA. These are values representative of what we expect when carrying out nuclear reactions investigations, for which we foresee typical beam energies E_p = 100–400 keV and typical currents I = 80–200 μA.

The resolution of particle peaks originating from reaction events is a combination of the electronic resolution quantified above, with the energy straggling due to the particles' path through the target, the foils in front of the detectors, and the dead layers in the silicon detectors. This energy straggling depends on the particle species, the energies, and the thickness of the different layers. Assuming a typical scenario of ∼ 3 MeV α-particles passing through ∼ 3.5 μm Mylar foils, the energy straggling according to SRIM is ∼35 keV FWHM. Combining the calculated straggling effects with the observed electronic resolution, we obtain an expected FWHM of approximately 85 keV. This is similar to the value of approximately 100 keV observed experimentally.

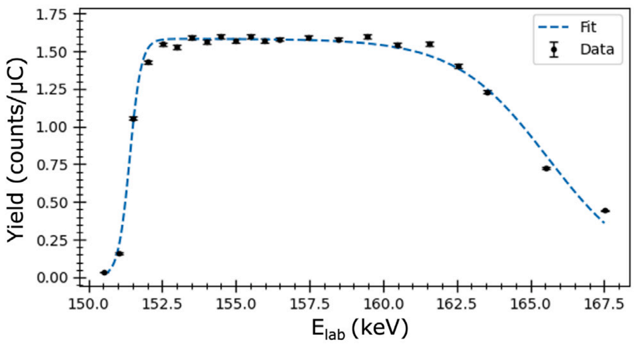

Fig. 12. A resonant scan of the ^{18}O (86.1% enrichment) target used to characterise the efficiency of the setup. The yields reported are for one MSPAD channel placed at 102.5°, as a function of the beam energy.

4.3. *Geometric efficiency*

The geometric efficiency of the detector array was determined with SimLUNA, a simulation tool based on GEANT4 (GEometry ANd Tracking) [26] developed by the LUNA collaboration [27]. The new detection array was included in SimLUNA with the silver dome, the protective foils with customisable thickness and the front section of the target holder, to account for shadow effects which could decrease the solid angle covered by the array. GEANT4 General Particle Source was used to simulate the isotropic emission of 10^7 α-particles with an energy of 2 MeV from a plane located at the target position, with the size of the beam spot measured experimentally (Section 2.3). The uncertainty associated with the simulated efficiency is conservatively estimated to be around ∼5%. The simulated efficiencies η_{sim} for a single detector placed at each of the five detection angles are reported in Table 1. For the MSPADs located at 102.5°, the efficiency of a single pad is indicated. To avoid excessive computational complexity, the simulation did not include the fine mesh grid, and simulated values were scaled for the 89% efficiency decrease observed experimentally (Section 3.5).

To validate the simulated efficiencies, data from the ^{18}O(p, α)^{15}N reaction were used. This reaction has a strong isotropic resonance [28] at E_p = 151.2 ± 0.3 keV with a well-known resonance strength of $\omega\gamma = 164.2 \pm 0.9_{stat}\,{}^{+12.1}_{-11.7}\,{}_{syst}$ meV [16], which emits ∼ 3.1 MeVα-particles. The resonance was used as a normalisation standard to derive the experimental detection efficiencies. This resonance was studied using an enriched ^{18}O (86.1%) target produced following the procedure in [29]. The resonance scan in thick-target conditions is shown in Fig. 12. The protective foils used for this measurement had a nominal thickness of 3.5 μm. The yields were then fitted with the semi-empirical function [16]:

$$f(\mathrm{E}) = \mathrm{H}\frac{1}{[1+\exp(\frac{\mathrm{E_R}-\mathrm{E}}{\delta_\mathrm{L}})]}\frac{1}{[1+\exp(\frac{\mathrm{E}-\mathrm{E_R}-\Delta\mathrm{E}}{\delta_\mathrm{R}})]} \tag{1}$$

where H is the plateau height, E_R is the resonance energy, $\delta_{L,R}$ are parameters describing the steepness of the plateau's rising and falling edges, and ΔE is the FWHM. In thick-target yield approximation, the parameter H corresponds to the maximum of the yield Y_{max} and can be linked to the resonance strength and to the experimental efficiency η_{exp} following [30]:

$$\eta_{exp} = \frac{2}{\lambda^2}\epsilon_{eff}\frac{\mathrm{Y_{max}}}{\omega\gamma} \tag{2}$$

where λ is the de Broglie wavelength, and ϵ_{eff} is the effective stopping power. We do not correct for any angular distribution in the centre-of-mass frame, and we assume it is isotropic as reported in the literature [28].

We calculated Y_{max} for each detector, and observed variations of up to 15% among detectors located at the same angle, exceeding

Table 1
Individual detector efficiencies for a given row of the detection array. The central angle with respect to the beam axis of the row is reported in the first column. The simulated efficiency includes the nominal 11% reduction due to the fine mesh grid (see Section 3.5) and a 5% uncertainty, whereas the experimental efficiency is derived from the ^{18}O(p, α)^{15}N data for two different configurations labelled (a) and (b) having different foil thickness, as described in the text.

Detector (Row angle)	η_{sim} (%)	$\eta^{\mathrm{a}}_{\mathrm{exp}}$ (%)	$\eta^{\mathrm{b}}_{\mathrm{exp}}$ (%)
Diode (102.1°)	0.43 ± 0.02	0.41 ± 0.03	0.35 ± 0.02
MSPAD (102.5°)	0.16 ± 0.01	0.16 ± 0.01	0.15 ± 0.01
Diode (125.7°)	0.45 ± 0.02	0.42 ± 0.03	0.42 ± 0.03
Diode (130.1°)	0.43 ± 0.02	0.38 ± 0.03	0.34 ± 0.02
Diode (154.5°)	0.44 ± 0.02	0.38 ± 0.03	0.38 ± 0.03

Table 2
Average tail-to-peak ratios of the α-peaks in the ^{18}O(p, α)^{15}N and ^{7}Li(p, α)α spectra. The adopted ratios were obtained from the average of all data acquired on these two reaction peaks, not simply the average of the two values shown. Uncertainties are obtained from the standard deviation of the values considered in the average.

Detector (Row angle)	$C_{\mathrm{tail}}/C_{\mathrm{peak}}$ (%)		
	^{18}O(p, α)	^{7}Li(p, α)	Adopted
Diode (102.1°)	19.7 ± 0.5	19.4 ± 2.4	19.5 ± 1.9
MSPAD (102.5°)	20.4 ± 0.4	20.4 ± 1.3	20.4 ± 1.1
Diode (125.7°)	6.5 ± 0.1	5.2 ± 1.0	5.6 ± 1.0
Diode (130.1°)	5.0 ± 0.1	4.3 ± 0.9	4.6 ± 0.8
Diode (154.5°)	4.5 ± 0.1	3.6 ± 0.5	3.9 ± 0.6

the expected uncertainty. We attribute these discrepancies to uneven geometric shadows of our very compact and complex setup on different detectors. Inserting measured yields in Eq. (2), with the resonance strength fixed to its literature value, we can derive an efficiency detector by detector, regardless of any shadow effects. Experimental uncertainties are evaluated combining the uncertainties on the literature resonance strength, which are given separately for separately contributions, with those on the experimental yields. Some of the literature uncertainties are in common with our current measurement and cancel out. Replacing the literature $\omega\gamma$ in Eq. (2) with its explicit formula we obtain

$$\eta_{\mathrm{exp}} = \frac{Y^{\mathrm{exp}}_{\mathrm{max}}}{Y^{\mathrm{lit}}_{\mathrm{max}}}\eta_{\mathrm{lit}} \tag{3}$$

where $Y^{\mathrm{exp}}_{\mathrm{max}}$ and $Y^{\mathrm{lit}}_{\mathrm{max}}$ are the maximum yields obtained in the present work and in the literature, respectively. The de Broglie wavelength term $2/\lambda^2$ cancelled out. The same type of target, produced using the same technique in the same setup, was used to obtain the literature value [16] of $\omega\gamma$ as in this work. Therefore, the stopping power ϵ_{eff} can also be cancelled out when evaluating uncertainties. Ultimately, the final uncertainty on the experimental efficiency η_{exp} can be derived by combining the statistical uncertainties on the two yields, a 3% systematic error on the collected charge, and the uncertainty on the literature efficiency. All literature uncertainties values are taken from [16].

The efficiency was re-measured as described above whenever we had major changes to the setup, and in particular whenever we had to change the foils, as dismounting and remounting the mesh-grid dome could potentially result in different geometric shadows of the setup. In Table 1 we report the results of the simulation for a detector on a given row (η_{sim}) and the average efficiency for a detector on the same row for two different experimental dome configurations, one with 3.5 μm foils mounted ($\eta^{\mathrm{a}}_{\mathrm{exp}}$) and one with 5 μm foils ($\eta^{\mathrm{b}}_{\mathrm{exp}}$). The agreement is good within uncertainties both between the simulation and the experimental data, and between the two data sets. This confirms the robustness of our efficiency values. When calculating a cross-section, we use the efficiency experimentally obtained for the specific dome configuration in which data were obtained. Note, however, that we did not observe any changes in the detection efficiency outside of the stated uncertainties. Also note that while the total efficiency theoretically achievable is 12.3%, due to some non-functional channels our total efficiency is typically around 9.7 ± 0.7%.

4.4. *Tail effects*

An example of the spectra acquired during the commissioning of this setup on the E_p = 151.2 keV resonance in the ^{18}O(p, α)^{15}N reaction is shown in Fig. 13 for two detection angles. The α-peak is observed at approximately 2500 keV. In addition to the main peak, the spectrum exhibits a pronounced tail-like structure developing towards lower energies. At larger angles, the effect is reduced and appears as a secondary structure rather than a smooth tail. The presence of this tail must be taken into account when deriving the number of detected reaction products from the counts in the associated peak. In the case of lower-energy peaks where a large part of the tail may be cut off by the minimum energy threshold, the tail-to-peak count ratio is required to properly evaluate the total number of emitted reaction products. Furthermore, the tail contribution is important to estimate the background beneath peaks that lie on the tail of other strong peaks. We believe that the observed tail arises primarily from geometric shadows. In addition, there may be contributions from known effects in charged-particle spectroscopy [31] using silicon detectors, such as Pulse Height Defects (PHD) and edge field distortions. In the case of PHD, charged particles undergo nuclear collisions with silicon atoms in the detector, and the resulting lattice recoil dissipates part of the deposited energy into non-ionising processes, thereby reducing the signal amplitude [32]. As for edge effects, particles interacting near the detector boundaries experience distortions of the electric field, which can lead to incomplete charge collection and consequently a reduced measured energy.

Quantifying the tail contribution is best done using an intense reaction, for which background contributions in the tail region can be neglected. Two reactions were selected for this purpose: ^{18}O(p, α)^{15}N and ^{7}Li(p, α)α. The E_p = 151.2 keV resonance in the ^{18}O(p, α)^{15}N reaction is ideally suited for this analysis, since it produces a single intense peak at a well-defined energy with a low-energy tail developing over a region where background is negligible. In this case, we arbitrarily defined the tail as the region from ∼ 300 to ∼2000 keV below the main peak, as shown in Fig. 13. The ^{7}Li(p, α)^{4}He reaction is another suitable case, as it produces a higher energy peak with a low-energy tail developing over a region free from background. The associated tail can be selected over a region with a similar energy width as the ^{18}O case. The tail-to-peak ratios obtained using these two reactions separately are compatible within their statistical uncertainties (Table 2). We adopted a tail-to-peak ratio obtained as the average of all values acquired on these two α-peaks across several spectra. Results are shown in Table 2 for the different detection angles. The reported uncertainties are purely statistical. The tail contribution is modest at the three highest angles, but becomes more significant at the lower ones, and cannot be neglected. An appropriate assessment of the tail-to-peak ratio will be crucial when studying signals from weak resonances with low expected count rate sitting on top of any contaminant peak tails. This will be the case for the nuclear astrophysical reaction measurements foreseen for this array.

5. Future prospects

We described the design, construction, and commissioning with and without beam of a new charged-particle detection array designed for use deep underground at the LUNA-400 accelerator. The background reduction afforded by the underground environment paired with the high beam intensities available from the LUNA-400 accelerator will allow us to probe a wide range of key nuclear reactions in quiescent astrophysical scenarios. The first reaction to be studied will be the ^{23}Na(p,

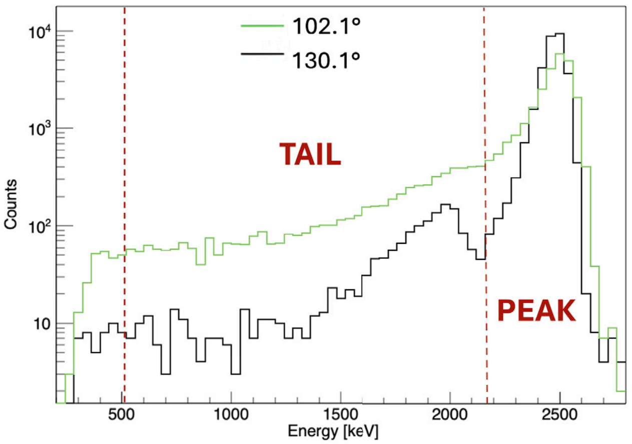

Fig. 13. Spectra obtained from the ^{18}O(p, α)^{15}N reaction on the plateau of the E_p = 151.2 keV resonance from a diode at 102.1° (green) and 130.1° (black). The dashed red lines indicate the boundaries of the regions arbitrarily defined as tail and peak, as used to determine the tail-to-peak ratio correction. Note the y-scale is logarithmic.

α)^{20}Ne reaction, of key importance for understanding the neon-oxygen anti-correlation problem in Globular Clusters [14]. Data analysis is in progress at the time of writing. For future investigations, we plan to upgrade the setup described here to include a large volume High-purity Germanium detector at zero degrees to carry out concurrent investigations of reactions emitting photons and charged particles. A first target for such a combined investigation will be the ^{27}Al(p, α)^{24}Mg and ^{27}Al(p, γ)^{28}Si reactions, which play a central role in our understanding of hot hydrogen burning in stars.

CRediT authorship contribution statement

L. Barbieri: Writing – review & editing, Writing – original draft, Visualization, Validation, Software, Methodology, Investigation, Formal analysis, Data curation. **J.J. Marsh:** Writing – review & editing, Writing – original draft, Methodology, Investigation, Formal analysis, Data curation. **C.G. Bruno:** Writing – review & editing, Writing – original draft, Supervision, Resources, Project administration, Investigation, Funding acquisition, Data curation, Conceptualization. **M. Aliotta:** Writing – original draft, Methodology, Funding acquisition. **C. Ananna:** Methodology. **F. Barile:** Methodology. **D. Bemmerer:** Resources, Methodology, Funding acquisition. **A. Best:** Methodology. **R. Biasissi:** Validation, Methodology, Data curation. **A. Boeltzig:** Writing – review & editing, Writing – original draft, Methodology. **R. Bonnell:** Methodology. **C. Broggini:** Funding acquisition. **A. Caciolli:** Methodology. **M. Campostrini:** Validation, Methodology, Data curation. **F. Casaburo:** Methodology. **F. Cavanna:** Methodology. **T. Chillery:** Validation, Methodology. **G.F. Ciani:** Methodology. **P. Colombetti:** Methodology. **A. Compagnucci:** Methodology. **P. Corvisiero:** Methodology. **L. Csedreki:** Methodology. **T. Davinson:** Methodology. **R. Depalo:** Methodology. **L. Dalla Vedova:** Methodology. **A. Di Leva:** Methodology. **Z. Elekes:** Software, Resources, Methodology. **F. Ferraro:** Resources, Methodology, Funding acquisition. **A. Formicola:** Supervision, Project administration, Investigation, Funding acquisition. **Zs. Fülöp:** Project administration, Methodology, Funding acquisition. **G. Gervino:** Methodology. **R.M. Gesuè:** Methodology. **G. Gosta:** Methodology. **A. Guglielmetti:** Methodology. **C. Gustavino:** Methodology. **Gy. Gyürky:** Resources, Methodology, Conceptualization. **G. Imbriani:** Methodology. **J. Jones:** Methodology. **M. Junker:** Methodology. **M. Lugaro:** Writing – review & editing, Writing – original draft, Supervision, Conceptualization. **E. Masha:** Methodology. **R. Menegazzo:** Methodology. **D. Mercogliano:** Methodology. **D. Piatti:** Methodology. **P. Prati:** Writing – review & editing, Writing – original draft, Methodology. **D. Rapagnani:** Methodology. **V. Rigato:** Supervision, Methodology, Funding acquisition. **D. Robb:** Visualization, Software, Methodology, Data curation. **M. Rossi:** Methodology. **R. Sariyal:** Methodology. **R.S. Sidhu:** Methodology. **J. Skowronski:** Methodology. **O. Straniero:** Writing – review & editing, Writing – original draft, Conceptualization. **T. Szücs:** Methodology. **S. Turkat:** Methodology. **M. Vagnoni:** Methodology. **S. Zavatarelli:** Methodology.

Declaration of competing interest

The authors declare that they have no known competing financial interests or personal relationships that could have appeared to influence the work reported in this paper.

Acknowledgements

This project was conducted with funding via the ELDAR UKRI ERC StG (EP/X019381/1). Peter Black from the University of Edinburgh's Nuclear Physics Lab, Andrew Dunlop and Giulia Gentile from the UoE College of Arts, as well as Donatello Ciccotti and the technical staff of the LNGS are gratefully acknowledged for their support. We acknowledge funding from the following: INFN, the European Union (ERC-CoG STARKEY, Grant No. 615604; ERC-StG SHADES, Grant No. 852016), the Deutsche Forschungsgemeinschaft (DFG, Grant No. BE 4100-4/1), the Helmholtz Association (Grant No. ERC-RA-0016), STFC (Grant No. ST/V001051/1 and No. ST/Y000293/1), the Hungarian National Research, Development, and Innovation Office (Grant No. NKKP ADVANCED 152233), and the European Collaboration for Science and Technology (COST Action ChETEC, Grant No. CA16117). E.M. acknowledges an Alexander von Humboldt postdoctoral fellowship. L. Cs. acknowledges the support of the Janos Bolyai Reserach Scholarship of the Hungarian Academy of Science. We acknowledge financial support under the Lendület Program LP2023-10 of the Hungarian Academy of Sciences and ChETEC-INFRA, Grant No. 101008324.

Data availability

Data will be made available on request.

References

[1] R.M. Gesuè, G.F. Ciani, D. Piatti, A. Boeltzig, D. Rapagnani, M. Aliotta, C. Ananna, L. Barbieri, F. Barile, D. Bemmerer, et al., First direct measurement of the 64.5 keV resonance strength in the o 17 (p, γ) F 18 reaction, Phys. Rev. Lett. 133 (5) (2024) 052701.

[2] J. Skowronski, R.M. Gesuè, A. Boeltzig, G.F. Ciani, D. Piatti, D. Rapagnani, M. Aliotta, C. Ananna, F. Barile, D. Bemmerer, A. Best, C. Broggini, C.G. Bruno, A. Caciolli, M. Campostrini, F. Cavanna, P. Colombetti, A. Compagnucci, P. Corvisiero, L. Csedreki, T. Davinson, R. Depalo, A. Di Leva, Z. Elekes, F. Ferraro, A. Formicola, Z. Fülöp, G. Gervino, A. Guglielmetti, C. Gustavino, G. Gyürky, G. Imbriani, M. Junker, M. Lugaro, P. Marigo, E. Masha, R. Menegazzo, V. Paticchio, R. Perrino, P. Prati, V. Rigato, L. Schiavulli, R.S. Sidhu, O. Straniero, T. Szücs, S. Zavatarelli, Advances in radiative capture studies at LUNA with a segmented BGO detector, J. Phys. G: Nucl. Part. Phys. 50 (4) (2023) http://dx.doi.org/10.1088/1361-6471/acb961.

[3] V. Mossa, K. Stöckel, F. Cavanna, F. Ferraro, M. Aliotta, F. Barile, D. Bemmerer, A. Best, A. Boeltzig, C. Broggini, et al., Nature 587 (7833) (2020) 210–213.

[4] A. Best, F.R. Pantaleo, A. Boeltzig, G. Imbriani, M. Aliotta, J. Balibrea-Correa, D. Bemmerer, C. Broggini, C.G. Bruno, R. Buompane, et al., Cross section of the reaction 18o (p, γ) 19F at astrophysical energies: The 90 keV resonance and the direct capture component, Phys. Lett. B 797 (2019) 134900.

[5] J. Skowronski, A. Boeltzig, G.F. Ciani, L. Csedreki, D. Piatti, M. Aliotta, C. Ananna, F. Barile, D. Bemmerer, A. Best, et al., Proton-capture rates on carbon isotopes and their impact on the astrophysical C 12/C 13 ratio, Phys. Rev. Lett. 131 (16) (2023) 162701.

[6] F. Ferraro, M.P. Takács, D. Piatti, F. Cavanna, R. Depalo, M. Aliotta, D. Bemmerer, A. Best, A. Boeltzig, C. Broggini, et al., Direct capture cross section and the E p=71 and 105 keV resonances in the Ne 22 (p, γ) Na 23 reaction, Phys. Rev. Lett. 121 (17) (2018) 172701.

[7] E. Masha, L. Barbieri, J. Skowronski, M. Aliotta, C. Ananna, F. Barile, D. Bemmerer, A. Best, A. Boeltzig, C. Broggini, et al., First measurement of the low-energy direct capture in ne 20 (p, γ) na 21 and improved energy and strength of the e cm=368 kev resonance, Phys. Rev. C 108 (5) (2023) L052801.

[8] L. Csedreki, G.F. Ciani, J. Balibrea-Correa, A. Best, M. Aliotta, F. Barile, D. Bemmerer, A. Boeltzig, C. Broggini, C.G. Bruno, A. Caciolli, F. Cavanna, T. Chillery, P. Colombetti, P. Corvisiero, T. Davinson, R. Depalo, A. Di Leva, Z. Elekes, F. Ferraro, E.M. Fiore, A. Formicola, Z. Fülöp, G. Gervino, A. Guglielmetti, C. Gustavino, G. Gyürky, G. Imbriani, Z. Janas, M. Junker, I. Kochanek, M. Lugaro, P. Marigo, E. Masha, C. Mazzocchi, R. Menegazzo, V. Mossa, F.R. Pantaleo, V. Paticchio, R. Perrino, D. Piatti, P. Prati, L. Schiavulli, K. Stöckel, O. Straniero, T. Szücs, M.P. Takács, F. Terrasi, S. Zavatarelli, Characterization of the LUNA neutron detector array for the measurement of the 13C(α, n)16o reaction, Nucl. Instrum. Methods Phys. Res. Sect. A: Accel. Spectrometers Detect. Assoc. Equip. 994 (2021) http://dx.doi.org/10.1016/j.nima.2021.165081.

[9] G.F. Ciani, L. Csedreki, D. Rapagnani, M. Aliotta, J. Balibrea-Correa, F. Barile, D. Bemmerer, A. Best, A. Boeltzig, C. Broggini, et al., Phys. Rev. Lett. 127 (15) (2021) 152701.

[10] D. Bemmerer, A. Boeltzig, M. Grieger, K. Gudat, T. Hensel, E. Masha, M. Osswald, B. Poser, S. Rümmler, K. Schmidt, J. Taín, A. Tarifeño-Saldivia, S. Turkat, A. Yadav, K. Zuber, Eur. Phys. J. A 61 (1) (2025) 19.

[11] L. Zhang, J. He, R.J. DeBoer, M. Wiescher, A. Heger, D. Kahl, J. Su, D. Odell, Y. Chen, X. Li, et al., Nature 610 (7933) (2022) 656–660.

[12] B. Gao, T.Y. Jiao, Y.T. Li, H. Chen, W.P. Lin, Z. An, L.H. Ru, Z.C. Zhang, X.D. Tang, X.Y. Wang, et al., Phys. Rev. Lett. 129 (13) (2022) 132701.

[13] A.C. Dombos, D. Robertson, A. Simon, T. Kadlecek, M. Hanhardt, J. Görres, M. Couder, R. Kelmar, O. Olivas-Gomez, E. Stech, F. Strieder, M. Wiescher, Phys. Rev. Lett. 128 (2022) 162701.

[14] A. Slemer, P. Marigo, D. Piatti, M. Aliotta, D. Bemmerer, A. Best, A. Boeltzig, A. Bressan, C. Broggini, C.G. Bruno, et al., Mon. Not. R. Astron. Soc. 465 (4) (2017) 4817–4837.

[15] M. Junker, A. D'Alessandro, S. Zavatarelli, C. Arpesella, E. Bellotti, C. Broggini, P. Corvisiero, G. Fiorentini, A. Fubini, G. Gervino, et al., Phys. Rev. C 57 (5) (1998) 2700.

[16] C.G. Bruno, D.A. Scott, A. Formicola, M. Aliotta, T. Davinson, M. Anders, A. Best, D. Bemmerer, C. Broggini, et al., Eur. Phys. J. A 51 (8) (2015) 94.

[17] C.G. Bruno, D.A. Scott, M. Aliotta, A. Formicola, A. Best, A. Boeltzig, D. Bemmerer, C. Broggini, A. Caciolli, F. Cavanna, et al., Phys. Rev. Lett. 117 (14) (2016) 142502.

[18] C.G. Bruno, M. Aliotta, P. Descouvemont, A. Best, T. Davinson, D. Bemmerer, A. Boeltzig, C. Broggini, A. Caciolli, F. Cavanna, et al., Phys. Lett. B 790 (2019) 237–242.

[19] M. Lugaro, A.I. Karakas, C.G. Bruno, M. Aliotta, L.R. Nittler, D. Bemmerer, A. Best, A. Boeltzig, C. Broggini, A. Caciolli, et al., Nat. Astron. 1 (2) (2017) 0027.

[20] O. Straniero, C.G. Bruno, M. Aliotta, A. Best, A. Boeltzig, D. Bemmerer, C. Broggini, A. Caciolli, F. Cavanna, G.F. Ciani, et al., The impact of the revised 17o (p, α) 14N reaction rate on 17o stellar abundances and yields, Astron. Astrophys. 598 (2017) A128.

[21] D. Rapagnani, O. Straniero, G. Imbriani, M. Aliotta, C. Ananna, F. Barile, L. Barbieri, D. Bemmerer, A. Best, A. Boeltzig, et al., Revision of the CNO cycle: Rate of o 17 destruction in stars, Phys. Rev. C 111 (2) (2025) 025805.

[22] A. Formicola, G. Imbriani, M. Junker, D. Bemmerer, et al., Nucl. Instrum. Methods Phys. Res. Sect. A: Accel. Spectrometers Detect. Assoc. Equip. 507 (3) (2003) 609–616.

[23] J.M. Meese, Neutron transmutation doping in semiconductors, in: Proc. 2nd Int. Conf. Columbia, Missouri, 1979.

[24] S.L. Thomas, T. Davinson, A.C. Shotter, A modular amplifier system for the readout of silicon strip detectors, Nucl. Instrum. Methods Phys. Res. 288 (1) (1990) 212–218.

[25] J.F. Ziegler, M.D. Ziegler, J.P. Biersack, Nucl. Instrum. Methods Phys. Res. Sect. B: Beam Interactions Mater. Atoms 268 (11–12) (2010) 1818–1823.

[26] S. Agostinelli, J. Allison, K. Amako, J. Apostolakis, H. Araujo, P. Arce, M. Asai, D. Axen, S. Banerjee, et al., Nucl. Instrum. Methods Phys. Res. 506 (3) (2003) 250–303.

[27] Z. Elekes, et al., in preparation.

[28] H. Lorenz-Wirzba, P. Schmalbrock, H.P. Trautvetter, M. Wiescher, C. Rolfs, W.S. Rodney, 1979, 313, (3), 346–362.

[29] A. Caciolli, D.A. Scott, A. Di Leva, A. Formicola, M. Aliotta, M. Anders, A. Bellini, D. Bemmerer, C. Broggini, M. Campeggio, et al., Eur. Phys. J. A 48 (10) (2012) 144.

[30] C. Iliadis, *Nuclear Physics of Stars*, Wiley-VCH Verlag GmbH, 2007.

[31] E. Steinbauer, G. Bortels, P. Bauer, J.P. Biersack, P. Burger, I. Ahmad, Nucl. Instrum. Methods Phys. Res. Sect. A: Accel. Spectrometers Detect. Assoc. Equip. 339 (1) (1994) 102–108.

[32] C.J. Bland, Appl. Radiat. Isot. 49 (9) (1998) 1225–1229.